ACADEMIA ROMÂNĂ
*Revue Roumaine de Chimie*
https://www.icf.ro/rrch/

*Rev. Roum. Chim.*,
**2024**, *69*(10–12), 595–603
DOI: 10.33224/rrch.2024.69.10-12.09

# SYNTHESIS AND CHARACTERIZATION OF ALUMINIUM OXIDE NANO ADSORBENTS *VIA* A SUSTAINABLE COMBUSTION METHOD FOR METHYL RED REMEDIATION

Ranjana GOSWAMI, Y. C. GOSWAMI* and Mahdi SHAHRESTASNI

Nano Research Lab, School of Sciences, ITM University Gwalior MP India 474001

*Received April 19, 2024*

The escalating contamination of water bodies due to organic pollutants necessitates innovative approaches for efficient remediation. Among these, aluminium metal oxide nanoparticles emerge as promising nano adsorbents for their exceptional adsorption properties. This manuscript details the synthesis of alumina nanoparticles ($Al_2O_3$ NPs) employing the combustion method, a viable approach for scalable production. The investigation delves into the structural, morphological, and optical attributes of $Al_2O_3$ NPs, employing diverse characterization techniques such as Fourier transform infrared (FTIR), X-ray diffraction (XRD), field-emission scanning electron microscopy (FE-SEM), and energy-dispersive X-ray spectroscopy (EDS). XRD analysis reveals a pore structure within the $Al_2O_3$ sample, with an average crystallite size of 68 nm, indicative of its nanoscale dimensions. Subsequently, the adsorption efficacy of the synthesized nanoparticles against methyl red (MR) absorption, a model organic pollutant, is evaluated. Remarkably, precipitation of $Al_2O_3$ NPs exhibits superior MR absorption, achieving a removal efficiency of 68% within a mere 100 minutes. This research underscores the potential of $Al_2O_3$ NPs synthesized via the combustion method as efficient nano adsorbents for the remediation of organic pollutants, offering insights for the development of advanced water purification technologies.

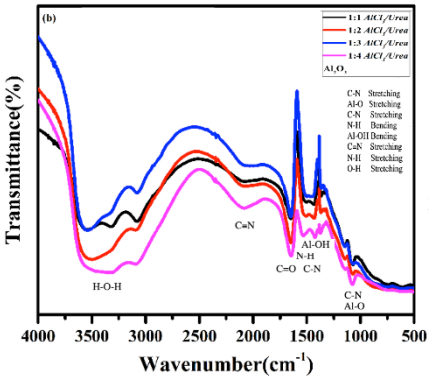


## INTRODUCTION

In recent years, the rapid advancement in nanoscale production techniques has spurred significant interest and exploration due to the unique properties inherent to nanomaterials.[1,2] These properties stem from phenomena such as quantum confinement and surface effects, resulting in nanoparticles exhibiting distinct chemical, electrical, optical, mechanical, and magnetic characteristics compared to their bulk counterparts.[3–6] Among nanomaterials, multi-phase nanoparticles within the size range of 1 to 100 nanometers have garnered particular attention for their diverse applications, including as adsorbents and catalysts, owing to their high surface area-to-volume ratio.[7] Many synthesis routes are being reported.[8–12]

Aluminum oxide, with the chemical formula $Al_2O_3$, encompasses various phases such as alpha, beta, gamma, and delta, each synthesized at different temperatures and possessing unique properties and applications.[13–15] Researchers are increasingly focused on developing hetero-structure photocatalysts incorporating different band gap materials to effectively eliminate organic pollutants, reflecting the growing interest in addressing environmental challenges through nanotechnology.[16,17]

* Corresponding authors: ycgoswami@gmail.com

Nanocrystalline metal oxides, including $Al_2O_3$, have witnessed a surge in applications across diverse fields such as medical sciences, capacitors, batteries, biological sensors, and biomedical applications due to their exceptional properties,[18–20] including enhanced surface area, porosity, stability, and low toxicity. In environmental applications, nano-sized metal oxides like $Al_2O_3$ have emerged as promising candidates for wastewater treatment owing to their high efficiency, cost-effectiveness, and photocatalytic potential.[21–25]

A significant amount of water has become contaminated with hazardous effluents such pesticides, dyes, and insecticides as a result of the numerous sectors' rapid development over the past few decades, which has a negative influence on the ecology and ecosystem. The contaminants released from the textile, pharmaceutical, dyeing, and tannery industries are among the numerous types of effluents, and they include toxic chemical dyes as well as other chemical compounds as significant pollutants.[26] One of the biggest threats to ecological stability and human health is water contamination from the dye industry.

Discharging sewage containing colours into water bodies not only results in unpleasant images, but also limits the amount of sunlight that can permeate the water. In addition to the fact that organic dyes are hazardous.[27–29] Thus, the removal of organic pollutants (dyes) is regarded as necessary and is divided into three categories: physical, chemical, and biological. Due to its viability and inexpensive approach, the photo-catalytic method has enormous significance in light of these factors.[30] These colours are made from a variety of chemicals, but the most popular combination is sulphuric acid with metals like copper, chromium, and other metallic elements. The three most common metal pollutants found in the population at risk are cadmium, lead, and chromium. Other dangerous contaminants include different metals (such as mercury, cobalt, arsenic, and nickel) and substances (such as nitrates, chlorine, and sulphur). After being merged, created in a reactor, filtered for impurities, and dried, dyes are blended. To start reactions, many additional solvents, additives, and chemical compounds are used.[31–33]

In this study, nano alpha-alumina was synthesized via the combustion process using aluminium salts as precursors and urea as a combustion agent, followed by calcination to produce nano alpha-alumina. The experimental parameters, including the concentration of the combustion agent and reaction sequence, were optimized to achieve maximum yield. To the best of our knowledge, this study presents a novel application of urea and aluminium salts for the synthesis of nano-alumina via the combustion method, with a focus on its potential application in the degradation of methyl red dye, thereby contributing to the development of efficient remediation strategies for organic pollutants in wastewater.

## EXPERIMENTAL

### Synthesis of Aluminium oxide nanoparticles

The synthesis of aluminium oxide nanoparticles involved utilizing aluminium chloride ($AlCl_3$), urea ($CH_4N_2O$), ethanol ($C_2H_6O$), and distilled water. Initially, 10 g of $AlCl_3$, serving as the oxidizer, was mixed with 20 ml of distilled water, and separately, 3 g of urea, serving as the fuel, was dissolved in 20 ml of distilled water. Both solutions were stirred using magnetic stirring for 60 minutes to ensure complete dissolution. These solutions were then combined in various ratios (A1 1:1; A2 1:2; A3 1:3; and A4 1:4) and stirred thoroughly to ensure homogeneity. The mixed solution was then transferred to a ceramic beaker.

The beaker containing the solution was placed into a muffle furnace and heated at 300°C for 3 hours, initiating the solution combustion process.[34–39] This was followed by increasing the temperature to 600°C and maintaining it for an additional 4 hours to promote the formation of aluminium oxide nanoparticles. After this heating process, the solid material was removed from the furnace and washed several times with ethanol and distilled water to remove any residual impurities. The washing was repeated until the wash water was clear. Finally, the washed material was dried in an oven at 100°C for 1 hour to eliminate any remaining solvent, resulting in the synthesis of pure aluminium oxide nanoparticles.

### Characterization studies

Particles were collected and characterized using optical, structural, and morphological studies. Optical absorption spectra were analyzed within the 300 nm-800 nm range using a Perkin-Elmer Lambda 25 UV/Vis-NIR spectrometer. Photoluminescence studies were performed with a Perkin Elmer LS55 spectrometer. The X-ray diffraction (XRD) pattern was obtained at room temperature using a Rigaku 350/600 mini Flex Smart Lab diffractometer with CuKα radiation (l = 1.5418 Å). The two-dimensional diffraction patterns were obtained over a range of 20 degrees –90 degrees. Surface morphology analysis of the nanoparticles was conducted using a TESCAN (USA) Model – MIRA 3 LMHFE scanning electron microscope (SEM) at IIT Roorkee.

### Batch adsorption experiment

Batch adsorption studies[40] were conducted by combining 0.2 g of each adsorbent (A1, A2, A3, and A4) with 25 ml of Methyl Red solution in 100 ml conical flasks. The flasks were

sealed during equilibration and positioned on a temperature-controlled, motorized orbital shaker. Absorption measurements were performed using a spectrophotometer with time interval of 10 minutes.

## RESULTS AND DISCUSSION

### Structural studies

The X-ray diffractograms of $Al_2O_3$ nanoparticles shown in Fig.1. The XRD diffractograms were used to analyse the structural properties and phase nature of the samples. The crystalline structure of the $Al_2O_3$ is observed. Debye Scherer's formula (Eq. 1)[41] is used to calculate the average crystallite sizes of the nanoparticles:

$$D = \frac{0.9\lambda}{\beta Cos\theta} \quad (1)$$

where D represents the crystallite size, β is the Full Width at Half Maximum (FWHM) intensity of the diffraction line in radians, λ is the X-ray wavelength (CuKa, l = 1.5406 Å), and θ is the Bragg's angle. The crystalline structure of the $Al_2O_3$ nanoparticles was determined from the XRD patterns illustrated in Fig. 1.

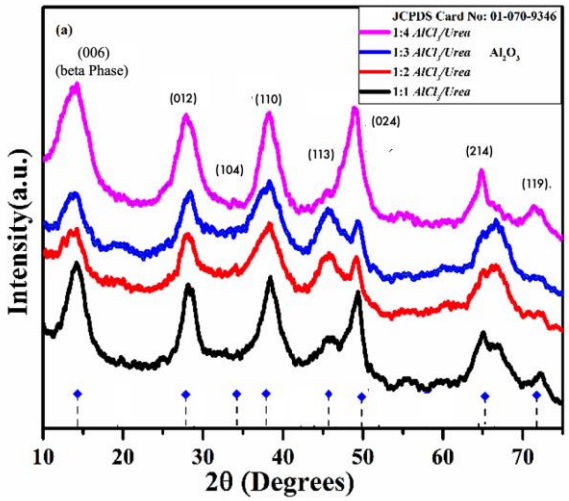


Fig. 1 – X-ray Diffractograms of $Al_2O_3$ nanoparticles (A1, A2, A3 and A4).

The XRD patterns obtained for the synthesized samples indicate the presence of α-$Al_2O_3$ as the predominant phase. This conclusion is based on the characteristic diffraction peaks observed at 2θ values of 25.58° (012), 35.15° (104), 37.80° (110), 43.38° (113), 52.55° (024), 57.50° (116), 66.40° (214), 68.18° (300), 76.85° (119), and 82.13° (1010). These peaks correspond well with the standard patterns for α-$Al_2O_3$ as per JCPDS Card No. 01-070-9346 and 46-1212.[42–44] In addition to the peaks corresponding to α-$Al_2O_3$, we observed unassigned peaks at lower angles, specifically around 15°. Such peaks may indicate the presence of intermediate phases, such as β-alumina or aluminium hydroxide compounds, which could form during the synthesis process and not fully transform into the final α-$Al_2O_3$ structure. The presence of these intermediates suggests that further optimization of the synthesis parameters may be necessary to achieve complete phase transformation.

The crystallite size calculation indicates that the average size is between 46 nm to 68 nm, with good crystalline character and no additional chemical impurities.[45] The XRD patterns also show significant peak broadening, particularly with increased amounts of urea in the synthesis process. Peak broadening in XRD attributed to factors, including reduced crystallite size and increased microstrain within the crystal lattice. In our synthesis method, urea acts as a fuel that influences the combustion reaction, leading to the formation of nanoparticles with smaller crystallite sizes and higher surface areas.[46,47] The addition of urea enhances the combustion process, resulting in a more vigorous reaction that produces finer particles. This effect is evident in the XRD patterns, where higher urea content correlates with broader peaks, indicating smaller crystallite sizes and potential lattice strain. The observed peak broadening is consistent with previous studies on solution combustion synthesis, where fuel-to-oxidizer ratios significantly impact the properties of the synthesized materials.[48–50]

Figure 2 shows Williamson–Hall plots[51] plotted (using Eq. 2) to determine the strain. The broadening of XRD peaks caused by the strain and the contribution of crystallite size can be summarized as follows:

$$Bhkl = \beta D + \beta\varepsilon \quad (2)$$

where $B_{hkl}$ = FWHM corrected, $\beta_D$ = Crystallite size, and $\beta_\varepsilon$ = strain induced broadening. The Williamson–Hall Equation can be simplified as follows:

$$\beta_{hkl}\, Cos\theta = k\lambda/D + 4\varepsilon Sin\theta_{hkl} \quad (3)$$

The size widening ($\beta_D$) is proportional to cos $\theta^{-1}$ and the strain broadening ($\beta_\varepsilon$) is related to tan θ. In order to compute the crystallite size and microstrain of the $Al_2O_3$ nanoparticles, a relationship between $\beta_{hkl}$ Cosθ and Sinθ is drawn for the prepared Sample

and is illustrated in Fig. 2. Particle size and strain calculation using Debye–Scherer formula and Williamson–Hall plot obtained and summarised in Table 1.

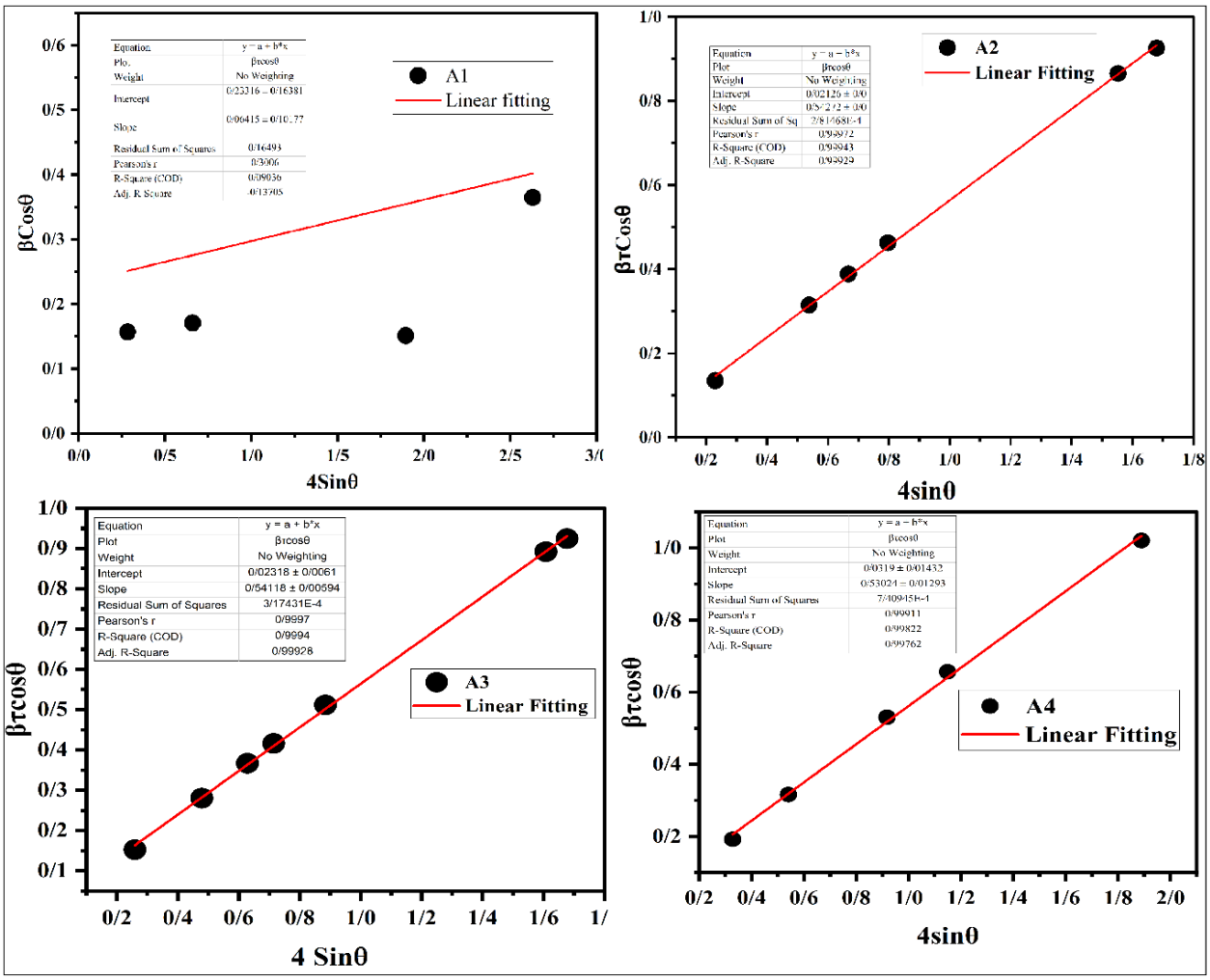


.Fig. 2 – Williamson–Hall plots of $Al_2O_3$ nanostructures (Samples eA1, A2, A3 and A4).

*Table 1*

Particle size and strain calculation using Debye–Scherer formula and Williamson–Hall plots

| Sample Code | FWHM | D=kλ/βCosθ | Intercept | Strain |
|---|---|---|---|---|
| **A1** | 0.360622926 | 62.110 | 0.23316 | 0.06415 |
| **A2** | 0.546488449 | 68.116 | 0.02126 | 0.54272 |
| **A3** | 0.535371271 | 62.474 | 0.02318 | 0.54118 |
| **A4** | 0.580293248 | 46.415 | 0.0312 | 0.53024 |

## FTIR Studies

To elucidate the chemical properties of the material, Fourier Transform Infrared (FTIR) spectroscopy was employed, with the resulting spectrum depicted in Fig. 3. Within the range of 500 to 4000 $cm^{-1}$, numerous peaks were observed. FTIR analysis of the synthesized nanoparticles revealed peaks at 1100 $cm^{-1}$ (C-N stretching and Al-O stretching), 1250 $cm^{-1}$–1600 $cm^{-1}$ (C-N stretching, N-H bending, and Al-OH bending), a large peak at 1700 $cm^{-1}$ (C=O stretching), a small peak at 2100 $cm^{-1}$ (C≡N stretching), a peak at 3100 $cm^{-1}$ (N-H stretching), and a broad hump between 3150 $cm^{-1}$–3500 $cm^{-1}$ (O-H stretching), indicating the presence of residual organic compounds and intermediate products from urea decomposition alongside the formation of aluminium oxide.[52–55]

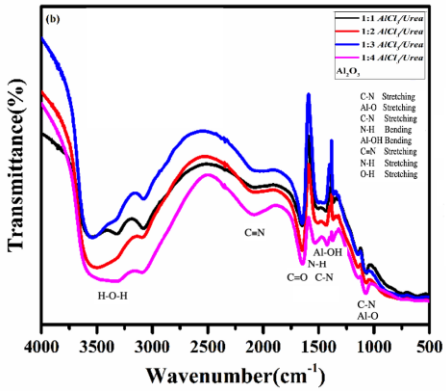


Fig. 3 – FTIR Spectra of $Al_2O_3$ nanostructures (A1, A2, A3 and A4).

## FE-SEM (Morphological studies)

The morphological investigation of $Al_2O_3$ nanoparticles was conducted through FE-SEM analysis, shown in Fig. 4. revealing notable changes associated with variations in the combustion agent (urea) ratio. Elevated urea ratios resulted in the development of a highly porous structure on the sample surfaces. This porosity is a typical characteristic of materials synthesized through combustion methods, which often result in gas release and pore formation. Figure 4(a) depicts the FE-SEM image of $Al_2O_3$ nanoparticles, showing evident cluster formation. As the urea ratio increased, a sponge-like nano porous structure emerged, as illustrated in Figs. 4b, 4c, and 4d for ratios 1:2, 1:3, and 1:4, respectively. Moreover, FE-SEM data indicate that increasing the temperature during synthesis led to a transition in particle morphology towards the sponge-like form. These observations highlight the influence of the urea ratio and temperature on the morphology and porosity of the synthesized nanoparticles.

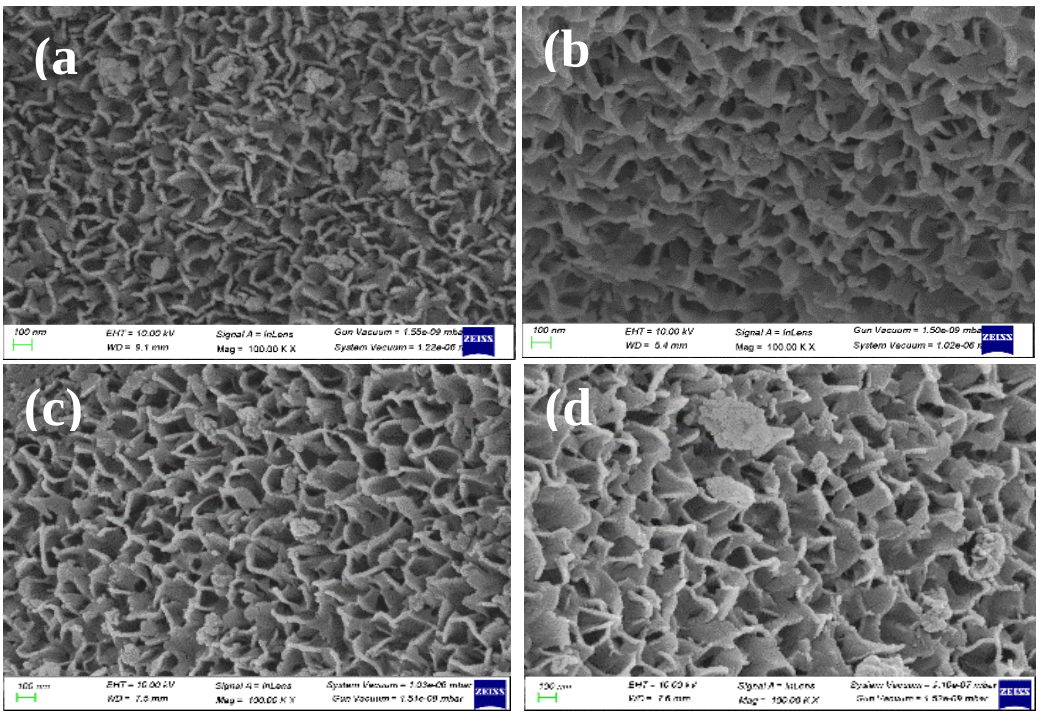


Fig. 4 – FE-SEM micrographs of aluminum oxide nanoparticles with different amounts of urea increasing from (a) to (d) respectively.

## Optical studies

### *UV–visible absorption spectra*

The UV-Vis absorption spectra of $Al_2O_3$ nanoparticle powder samples, shown in Fig. 5a, were recorded over the wavelength range of 200 nm–600 nm. The spectra reveal significant ultraviolet absorption across all samples, with two prominent regions of absorption peaks. The first series of absorption peaks observed between 200 nm and 250 nm, is attributed to the electronic transitions related to the oxygen 2p to aluminium 3d charge transfer. This transition is characteristic of the fundamental absorption edge in $Al_2O_3$, where the high energy UV light excites electrons from the oxygen's non-bonding orbitals to the conduction band of aluminium oxide. The variation in peak intensity across samples suggests differences in the nanoparticle size and surface states, which affect the transition probability. The second series of

absorption peaks, located between 350 nm and 400 nm, corresponds to the intrinsic band-to-band transitions within the aluminium oxide structure. These peaks are associated with electron transitions from the valence band to the conduction band of $Al_2O_3$. The increase in absorption intensity with higher urea molar ratios indicates enhanced electronic transitions, likely due to increased particle surface area or improved crystallinity. Overall, the UV-Vis spectra demonstrate strong absorption within the UV range (200 nm–400 nm), primarily due to these electronic transitions. The enhanced absorption with increased urea molar ratio suggests improved optical properties and electronic structure of the $Al_2O_3$ nanoparticles.[56,57]

***PL Studies***

The photoluminescence (PL) spectra of $Al_2O_3$ samples were carried out and shown in Fig. 5b. The PL spectra reveal two distinct emission features: a minor luminescence peak in the ultraviolet region, ranging from 275 nm to 300 nm, and a more prominent peak at longer wavelengths, between 325 nm and 400 nm. The peak observed between 275 and 300 nm is attributed to the intrinsic electronic transitions related to defects and oxygen vacancies within the $Al_2O_3$ nanomaterials. These emissions are indicative of recombination processes involving electron-hole pairs trapped at defect sites or surface states. The shift of this peak towards shorter wavelengths with increasing urea molar ratio suggests the creation of more localized energy states or defects within the $Al_2O_3$ matrix, which can trap and subsequently release energy as UV luminescence.

The larger peak at nm 325 to 400 nm can be associated with the band-to-band transitions within the $Al_2O_3$ structure. As the molar ratio of urea increases, the enhanced intensity and shift of this peak towards higher wavelengths reflect improved crystallinity or altered electronic band structure of the nanoparticles. This shift indicates a lengthening of the radiative recombination lifetime of the electron-hole pairs, which reduces non-radiative recombination processes and enhances the observed PL emission. The presence of these UV emissions is indicative of the good luminescence behaviour of $Al_2O_3$ nanomaterials, which is further influenced by the energy band modifications introduced by varying the urea molar ratio. The observed phenomena suggest that the increased molar ratio of urea affects both the defect-related and band-edge emission processes, leading to notable changes in the luminescence characteristics.

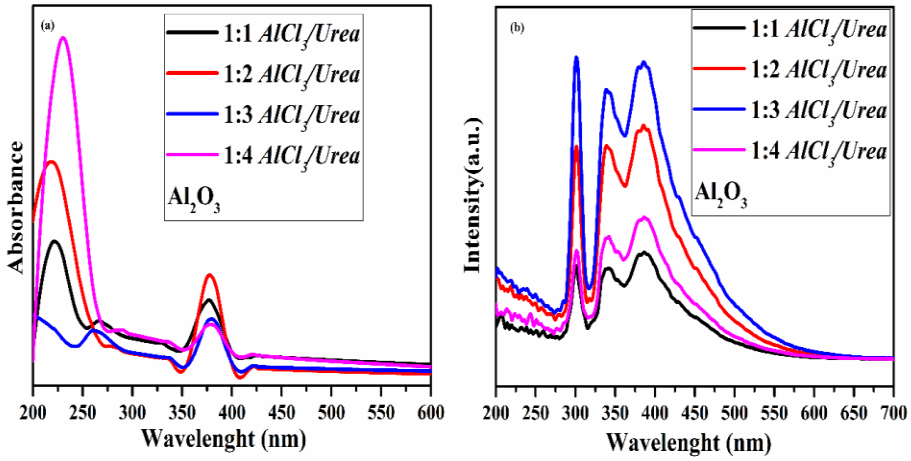


Fig. 5 – (a) Absorption spectra of $Al_2O_3$ nanoparticles; (b) Photoluminescence Spectrum of $Al_2O_3$ nanostructures A1, A2, A3 and A4, respectively.

## Tuac Plot

The Tauc plot, illustrated in Fig. 6, depicts $(\alpha h\nu)^2$ versus $h\nu$ for the $Al_2O_3$ samples. The estimated band gaps for the samples range from 3.3 eV to 4.7 eV. Despite significant variations in the $AlCl_3$-to-Urea ratio, which influences the concentration of the components, the observed bandgap values show notable differences. This variation suggests that there have been substantial changes in the electronic structure of $Al_2O_3$.

The bandgap values determined from the Tauc plots for the four samples are as follows: 3.39 eV for Sample A1, 4.71 eV for Sample A2, 4.11 eV for Sample A3, and 4.75 eV for Sample A4. These differences in bandgap energy indicate that modifications in the synthesis conditions have a marked impact on the electronic properties of $Al_2O_3$.

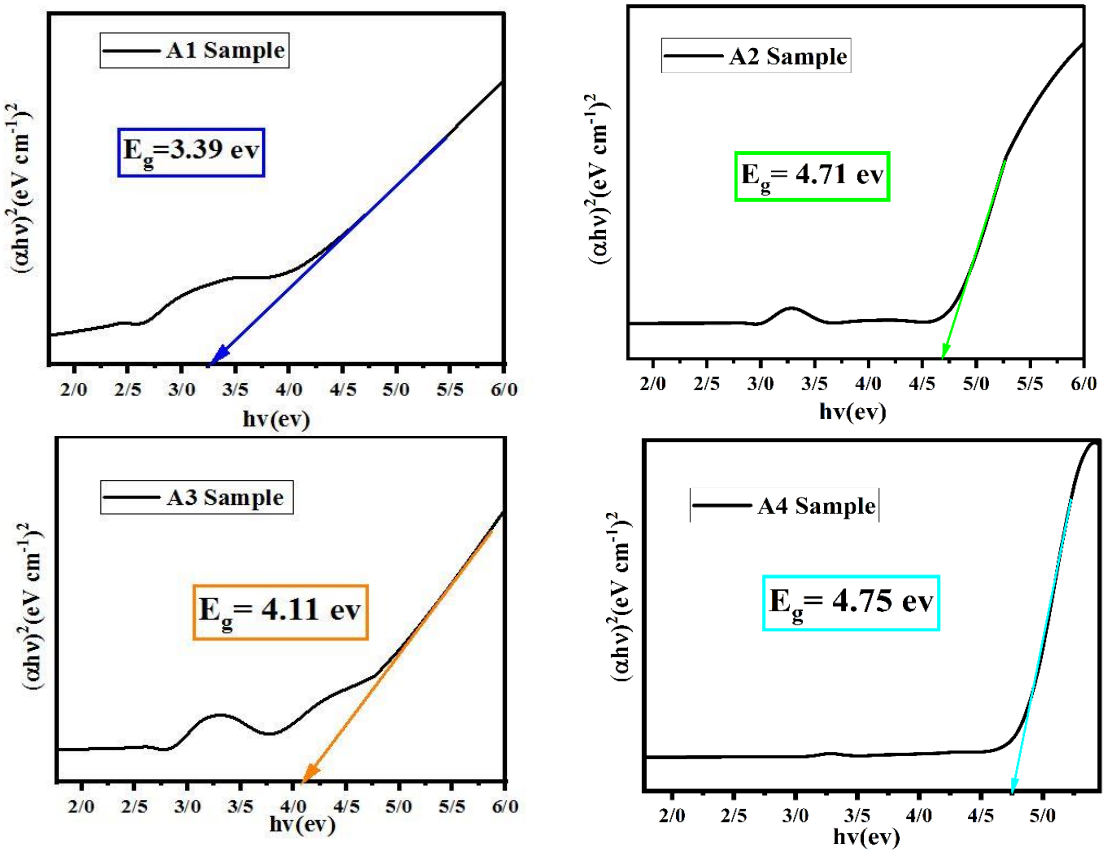


Fig. 6 – $(\alpha h\nu)^2$ versus hν for the $Al_2O_3$ samples (A1–A4 respectively).

## Absorption studies

With the help of the aluminum oxide absorbance (A1) Sample1, (A2) Sample2, (A3) Sample3, and (A4) Sample4, the Methyl red dye underwent absorbance studies have been carried out.

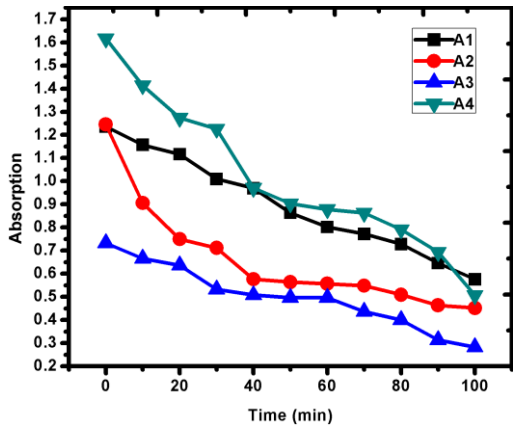


(a)

Fig. 7 – Absorption curve of Methyl Red in the presence of $Al_2O_3$ Nano absorbance.

Figure 7 shows the dye absorption curves when a nano absorbance is added to the dye solution. At 391 nm, the dye solution's maximum absorption of 1.65 was measured. The pace of reaction increases as the urea ratio rises because a low urea ratio in an $Al_2O_3$ nano absorbance exhibits a lower degradation curve than a high urea ratio does. The combustion reagent materials cause differences in the deterioration curve by speeding up the recombination of electrons and holes. These electrons and holes disintegrate from the water as a result of their reaction with the dye solution. The coulombs force or attraction between the dye and the nano absorbance causes a drop in dye concentration. The percentage of dye concentration decreases upon addition of nano absorbance in dye solutions. The fluctuations appearing in the decay curves are due to the increased recombination rate of electrons and holes due to the increased burning material in the basic compound. These electrons and holes react with the dye solution and are decomposed from the water.

The dye concentration is reduced by Coulomb forces or attractive forces between the dye and the Nano adsorber. Percentage degradation graph shwn in Fig. 8. The rate of absorption follow the order.

A4 >A2 >A3 >A1

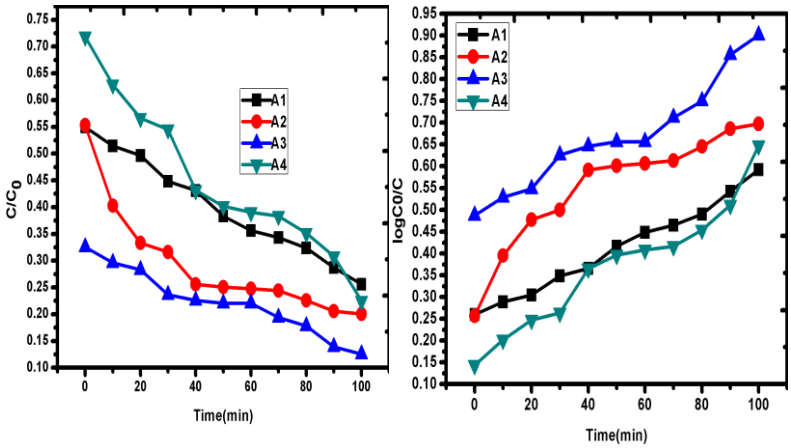


(b) (c)

Fig. 7 – b) $C/C_0$ with time and c) log $C_0/C$ with time Curve ofc Methyl red in the presence of Nano absorbance (A1) Sample1 (A2) Sample2 (A3) Sample3 (A4) Sample4 respectively.

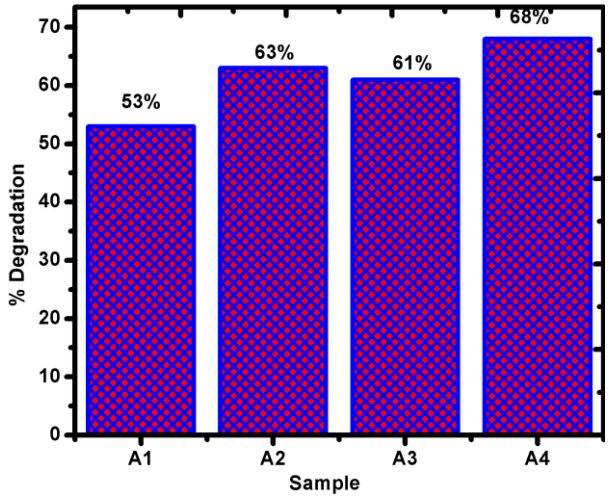


Fig. 8 – Degradation percentage graph.

## CONCLUSIONS

The effective synthesis of aluminium oxide nanoparticles ($Al_2O_3$) using the solution combustion method resulted in an average particle size of 68 nm with a a $Al_2O_3$ structures. The Alumina nanoparticles' conformation was revealed by the FTIR spectrum. Alumina nanoparticles absorb a high amount of Methyl Red dye. Among all the various samples Sample A4 was the best absorber material for the degradation of Methyl Red, with a percentage of 68% after 140 minutes. The findings indicate that $Al_2O_3$ nanostructures are a viable material for effective nano-adsorbent applications

*Acknowledgements.* Authors are thankful to PC-Ray center of research, ITM University Gwalior for providing characterizations facilities like UV-Vis spectroscopy, PL FTIR. The work has been funded by the MP Council of Science and Technology (MPCST), DST Sanctioned order Number A/RD/RP-2/305/2021-2022 (R&D Files number. A/RD/RP-2/305) and seed money by ITM University Gwalior.

## REFERENCES

1. R. X. Yang, C. A. McCandler, O. Andriuc, M. Siron, R. Woods-Robinson, M. K. Horton and K. A. Persson, *ACS Nano.*, **2022**, *16*, 19873–19891.
2. S. Nagaich and Y. C. Goswami, "Shor's Algorithm for Quantum Numbers Using MATLAB Simulator", *Fifth International Conference on Advanced Computing & Communication*, **2015**.
3. D. F. Niero, O. R. K. Montedo and A. M. Bernardin, *Mater. Sci. Eng.: B*, **2022,** *280*, 115690–115700.
4. K. K. Anna, N. K. R. Bogireddy and V. Agarwal, *Mater. Lett.*, **2022**, 317.
5. L. Zhonglin, D. Wang, F. Lv, J. Chen, C. Wu, Y. Li, J. Shen and Y. Li *Materials (Basel)*, **2022,** *15*, 970.
6. M. Makarem, T. Roostaei and M. Bonyadi, *Top. in Catal.*, **2022**, 67, 1417–1417.
7. M. Farahmandjou and N. Golabiyan**,** *Int. J. Bio-Inorg. Hybrid Nanomater.*, **2016**, *5*, 73–77.
8. R. Singh, D. Kumar, Y. C. Goswami and R. Sharma, *Arab. J. Chem.*, **2019,** *12*, 1537–1544.
9. D. Pal, G. Singh, Y. C. Goswami and V. Kumar *J. Mater. Sci.: Mater. Electron.*, **2019**, *30*, 15700–15704.
10. R. Sharma, R. Singh, Y. C. Goswami, V. Kumar and D. Kumar, *J. Aust. Ceram. Soc.*, **2021**, *57*, 697–703.

11. Y. C. Goswami, R. Singh, R. Sharma and D. Kumar, *Contemporary Eng. Sci.*, **2019**, *5*, 1–8.
12. R. Singh, D Kumar, Y. C. Goswami and R. Goswami, *Arab. J. of Chem*., **2019**, *12*, 1537–1544.
13. R. K. Mylavarapu, *Rasayan J. Chem.*, **2017**, *10*, 716–722.
14. V. P. Dhawale, V. B. Khobragade and S. D. Kulkarni, *Int. J. Environ. Chem.*, **2018**, *2*, 10–17.
15. R. Gusain, K. Gupta, P. Joshi and O. Khatri, *Adv. Colloid Interface Sci.*, **2019**, *272*, 102009.
16. S. Ali, Y. Abbas, Z. Zuhra and Ian S. Butler, *Nanoscale Advances*, **2019**, *1*, 213–218.
17. K. Rajagopalan, K. Revathi, B. Revathi, V. Senthilkumar, M. Kumar, K. Batoo, K. Saminathan and P. Palanisamy, *Materials Today: Proc.*, **2020**, *48*, 160–163.
18. S. Thanigachalam, M. Pathak and K. I. Sathiyanarayanan, *J. Coord. Chem.*, **2022**, *75*, 2189–2213.
19. L. Thangavelu, G. R. Veeraragavan, S. K. Mallineni, E. Devaraj, R. P. Parameswari, N. H. Syed, K. Dua, D. K. Chellappan, S. R. Balusamy and U. K Bhawal, *Bioinorg. Chem. Appl.*, **2022**, 1946724.
20. H. Kadtem, W. I. Yahya, N. A. Ridha and E. H. Sahap, *Int. J. Health Sci.*, **2022**, 7613–7620.
21. C. Bakouan and I. Z. Guel, *Processes*, **2022**, *10*, 1826.
22. S. D. Jahromi, D. Karami and N. Mahinpey, *J. Environ. Chem. Eng.*, **2022**, *10*, 107204.
23. R. Wahab, M. Alam, *Inorg. Chem. Comm.*, **2023**, 147.
24. K. Parida, A. C. Pradhan, J. Das and N. Sahu, *Mater. Chem. Phys.*, **2009**, *113*, 244–48
25. M. V. V. T. Poiyamozhi and J. Thivya, *J. Mater. Sci.: Mater. Electronics*, **2022**, *33*, 19462–19476.
26. J. Briffa, E. Sinagra and R. Blundell, *Heliyon*, **2020**, *6*, e04691.
27. M. Qa and K. Ms, *J. Pollution Effects & Control*, **2016**, *5*, 179.
28. H. Zhang , X. Zhou, L. Wang, W. Wang and J. Xu, *Ecotoxicol. Environ. Safety*, **2018**, *164*, 181–188.
29. D. Domyati, *Ceramics Int.*, **2023**, *49*, 1464–1472.
30. T. Ilame and A. Ghosh, *Management Environ. Quality: An Int. J.*, **2021**, *33*, 451–477.
31. S. Banerjee, S. Dubey, R. K. Gautam, M. C. Chattopadhyay and Y. C. Sharma, *Arab. J. Chem.*, **2019**, *12*, 5339–5354.
32. P. Punia, M. Naagar, S. Chalia, B. Bavelo, P. Thakur and A. Thakur, *Ceramics Int.*, **2021**, *47*, 1526–1550.
33. K. C. Patil, S. T. Aruna and T. Mimani, *Curr. Opinion in Solid State and Mater. Sci.*, **2002**, *6*, 507–512. https://doi.org/10.1016/S1359-0286(02)00120-4.
34. A. S. Mukasyan and P. Dinka, *Int. J. Self-Propagating High-Temp. Syn.*, **2007**, *16*, 23–35. https://doi.org/10.3103/S1061386207010057
35. K. Jain, A. J. Kora and J. Arunachalam, *Mater. Lett.*, **2009**, *63*, 2406-2408. https://doi.org/10.1016/j.matlet.2009.08.035
36. B. Moghaddam, M. Salavati-Niasari and M. Bazarganipour, *J. Sol-Gel Sci. Technol.*, **2018**, *85*, 673–682. https://doi.org/10.1007/s10971-018-4695-6
37. J. Singh, A. Kumar and K. H. Kim, *Ceramics Int.*, **2022**, *46*, 27282–27302. https://doi.org/10.1016/j.ceramint.2020.07.184
38. L. Renuka, R. P. George and J. Philip, *Mater. Sci. Eng.: B*, **2021**, *271*, 115309. https://doi.org/10.1016/j.mseb.2021.115309
39. N. Abdus-Salam and S. K. Adekola, *Appl. Water Sci.*, **2018**, *8*, 222. https://doi.org/10.1007/s13201-018-0867-7
40. N. Kumar, L. P. Purohit and Y. C. Goswami, *Physica E: Low-dimensional Systems and Nanostructures*, **2016**, *83*, 333–338. https://doi.org/10.1016/j.physe.2016.04.025.
41. Y. C. Goswami, J. B. Kaundal, S. Begzaad and R. K. Tiwari, *J. Iran. Chem. Soc.*, **2023**, *20*, 1681–1697.
42. M. Mohammed, Z. T. Khodair and A. A. Khadom, *Ceramics Int.*, **2020**, *46*, 26945–26955.
43. M. Boumaza, *J. Solid State Chem.*, **2009**, *182*, 1171–1176.
44. M. Khan, N. K. Janjua, S. Khan, I. Qazi, S. Ali and T. S. Algarni, *Coatings*, **2021**, *11*, 257.
45. M. Yan, J. Liu and H. Yan, *J. Alloys and Compounds*, **2020**, *845*, 155925.
46. D. Li, X. Sun and H. Song, *Mater. Chem. Phys.*, **2019**, *230*, 225.
47. S. Basu, A. Kumar and R. Kumar, *J. Mater. Sci.*, **2017**, *52*, 3425–3433.
48. K. C. Patil, S. T. Aruna and T. Mimani, *Curr. Opinion Solid State Mater. Sci.*, **2002**, *6*, 507–512.
49. A. P. Rao, V. S. Kumar and Y. P. Babu, *Ceramics Int.*, 2018, *44*, 14284-14292. https://doi.org/10.1016/j.ceramint.2018.04.059
50. Y. C. Goswami, J. B. Kaundal, S. Begzaad and R. K. Tiwari *J. Iran. Chem. Soc.*, **2023**, *20*, 1681–1697. https://doi.org/10.1007/s13738-023-02789-5.
51. V. D. Zhuravlev, V. G. Bamburov, A. R. Beketov, L. A. Perelyaeva, I. V. Baklanova, O. V. Sivtso, V. G. Vasil'ev, E. V. Vladimirova, V. G. Shevchenko and I. G. Grigorov, *Ceram. Int.***, 2013,** *39*, 1379–1384.
52. N. Y. Topsoe and H. Topsoe, *J. Catal.*, **1993,** *139*, 631–640.
53. A. M. Tankari, K. Medjnoun, M. Nouiri, O. Briot, S. Juillaguet, H. Peyre, M. Belaqziz and K. Djessas, *Mater. Lett*., **2023,** *353*, 135230.
54. P. M. Schaber, J. Colson, S. Higgins, D. Thielen, B. Anspach and J. Brauer, *Thermochimica Acta*, **2004**, *424*, 131–142.
55. A. S. Jbara, Z. Othaman, A. A. Ati and M. A. Saeed, *Mater. Chem. Phys.*, **2016**, *188*, 24–29.
56. M. N. Nduni, A. M. Osano and B. Chaka, *Cleaner Eng. Technol.*, **2021**, *3*, 100108.